Monthly Notices of the ROYAL ASTRONOMICAL SOCIETY

MNRAS **467,** 936–949 (2017) doi:10.1093/mnras/stx155
Advance Access publication 2017 January 19

A study of halo and relic radio emission in merging clusters using the Murchison Widefield Array

L. T. George,[1⋆] K. S. Dwarakanath,[1⋆] M. Johnston-Hollitt,[2] H. T. Intema,[3] N. Hurley-Walker,[4] M. E. Bell,[5,6] J. R. Callingham,[5,6,7] B.-Q. For,[8] B. Gaensler,[7] P. J. Hancock,[4,6] L. Hindson,[9] A. D. Kapińska,[6,8] E. Lenc,[7] B. McKinley,[10] J. Morgan,[4] A. Offringa,[11] P. Procopio,[10] L. Staveley-Smith,[8] R. B. Wayth,[4,6] C. Wu[8] and Q. Zheng[2]

[1]*Raman Research Institute, Bangalore 560080, India*
[2]*School of Chemical and Physical Sciences, Victoria University of Wellington, PO Box 600, Wellington 6140, New Zealand*
[3]*Leiden University, PO Box 9500, NL-2300 RA Leiden, the Netherlands*
[4]*International Centre for Radio Astronomy Research, Curtin University, Bentley, WA 6102, Australia*
[5]*CSIRO Astronomy and Space Science (CASS), PO Box 76, Epping, NSW 1710, Australia*
[6]*ARC Centre of Excellence for All-sky Astrophysics (CAASTRO), 44 Rosehill Street, Redfern, NSW 2016, Australia*
[7]*Sydney Institute for Astronomy, School of Physics, The University of Sydney, NSW 2006, Australia*
[8]*International Centre for Radio Astronomy Research, University of Western Australia, Crawley, WA 6009, Australia*
[9]*Centre for Astrophysics Research, School of Physics, Astronomy and Mathematics, University of Hertfordshire, College Lane, Hatfield AL10 9AB, UK*
[10]*School of Physics, The University of Melbourne, Parkville, VIC 3010, Australia*
[11]*ASTRON, NL-7990 AA Dwingeloo, the Netherlands*

Accepted 2017 January 17. Received 2017 January 8; in original form 2016 September 21

ABSTRACT

We have studied radio haloes and relics in nine merging galaxy clusters using the Murchison Widefield Array (MWA). The images used for this study were obtained from the GaLactic and Extragalactic All-sky MWA (GLEAM) Survey which was carried out at five frequencies, viz. 88, 118, 154, 188 and 215 MHz. We detect diffuse radio emission in eight of these clusters. We have estimated the spectra of haloes and relics in these clusters over the frequency range 80–1400 MHz; the first such attempt to estimate their spectra at low frequencies. The spectra follow a power law with a mean value of $\alpha = -1.13 \pm 0.21$ for haloes and $\alpha = -1.2 \pm 0.19$ for relics, where $S \propto \nu^{\alpha}$. We reclassify two of the cluster sources as radio galaxies. The low-frequency spectra are thus an independent means of confirming the nature of cluster sources. Five of the nine clusters host radio haloes. For the remaining four clusters, we place upper limits on the radio powers of possible haloes in them. These upper limits are a factor of 2–20 below those expected from the $L_{\rm X}$–$P_{1.4}$ relation. These limits are the lowest ever obtained and the implications of these limits to the hadronic model of halo emission are discussed.

Key words: radiation mechanisms: non-thermal – techniques: interferometric – galaxies: clusters: general – galaxies: clusters: intracluster medium – radio continuum: general – X-rays: galaxies: clusters.

1 INTRODUCTION

According to the hierarchical model for structure formation, galaxy clusters are formed as a result of several successive mergers between smaller sub-clusters. These mergers are extremely powerful events that can release an enormous amount of energy ($\sim 10^{63}$–10^{64} erg, Hoeft et al. 2008) into the surrounding intracluster medium (ICM). A fraction of this energy could be used to amplify magnetic fields in clusters (Carilli & Taylor 2002; Subramanian, Shukurov & Haugen 2006) and/or accelerate relativistic electrons in the ICM (Brunetti et al. 2001; Petrosian 2001) as a result of which synchrotron radiation could be produced in the ICM.

This extended ($\sim$ Mpc), diffuse ($\sim$ few mJy arcmin^{-2} at 1.4 GHz) radio emission from galaxy clusters which is not associated with any galaxy or compact object, but rather from the ICM gas itself comes in two forms – *radio haloes* and *radio relics* (Feretti et al. 2012; Brunetti & Jones 2014). Radio haloes are found in the central regions of clusters while the relics are found mostly near the peripheries of clusters, towards the edges of the X-ray emission.

⋆ E-mail: lijo@rri.res.in (LTG); dwaraka@rri.res.in (KSD)

Haloes usually have a smoother, circular morphology while relics are usually elongated and arc-like.

Clusters which host these haloes and relics are rare in the Universe. Below a redshift of $z = 0.2$, only ∼5 per cent of all galaxy clusters host these objects (Giovannini, Tordi & Feretti 1999). In a study of highly X-ray luminous clusters ($L_X \gtrsim 10^{45}$ erg s^{-1}) with $0.2 < z < 0.4$, (Venturi et al. 2007, 2008, and its follow-up by Kale et al. 2013) found that 38 per cent of galaxy clusters hosted radio haloes. Additionally, highly X-ray luminous galaxy clusters are also expected to have higher radio powers as well (Liang et al. 2000; Bacchi et al. 2003; Cassano, Brunetti & Setti 2006; Brunetti et al. 2007, 2009; Rudnick & Lemmerman 2009). However, most previous efforts to increase the number of haloes and relics have concentrated on X-ray luminous clusters and there has yet to be a completely unbiased search for diffuse cluster emission.

Relics are believed to trace the outward going shocks produced at the time of cluster merger. The theory that explains this mechanism, diffusive shock acceleration theory (Blandford & Eichler 1987; Jones & Ellison 1991; Ensslin et al. 1998) suggests that electrons in the ICM suffer multiple collisions across the two fronts of the outward going shock as a result of which they get accelerated diffusively. Clusters with double relics i.e. relics that are located on opposite ends of the cluster centre and trace the outgoing shocks are the best examples in support of this theory. However, recent analysis (Vazza & Brüggen 2014; Vazza et al. 2015, 2016) suggests that this might not be completely true. There are still large uncertainties on the mechanism by which the electrons can be accelerated or reaccelerated by such low Mach number shocks as those observed in clusters.

The origin of radio haloes is also not well understood. The basic problem with the existence of Mpc-sized radio haloes is that the synchrotron lifetimes of the radiating electrons is about 10 times smaller than their diffusion time-scales over the sizes of radio haloes. A consequence of this is that relativistic electrons cannot be produced in the active galaxies in clusters and transported all over the cluster. The existence of Mpc-sized haloes appears to imply *in situ* acceleration. The most popular model used to explain them is that of *turbulent acceleration* or the *primary* model (Brunetti et al. 2001; Petrosian 2001). According to this model, the electrons in the ICM are accelerated as a result of turbulence which is generated in the aftermath of a cluster merger. A 'proof' of such a scenario is the fact that clusters with disturbed morphologies are known to host radio haloes than relaxed clusters (Buote 2001; Cassano et al. 2010). An alternative to this model is the *hadronic* or *secondary* model (Dennison 1980; Blasi & Colafrancesco 1999; Pfrommer & Enßlin 2004) according to which inelastic collisions between relativistic protons and thermal protons in the ICM produces pions which decay to produce electrons and gamma rays. The lack of gamma-ray detections in galaxy clusters (Aharonian et al. 2009a,b; Ackermann et al. 2010; Aleksić et al. 2010) is a major shortcoming of this model. It is also claimed that the synchrotron emission from the secondary model is a factor of 10 lower than that from the primary model.

Radio haloes are known to exhibit an empirical correlation between the radio power of the halo at 1.4 GHz and the X-ray luminosity of the galaxy cluster that hosts the halo (Feretti 2000; Liang et al. 2000; Govoni et al. 2001b; Bacchi et al. 2003; Brunetti et al. 2007, 2009). Recent Giant Metrewave Radio Telescope (GMRT) observations of galaxy clusters (Venturi et al. 2007, 2008) also found that galaxy clusters show a *bi-modal* nature in the L_X–$P_{1.4}$ plot. In many clusters where no radio halo was detected, upper limits to the halo emission were placed that are a factor of 2–3 below the expected radio power. While it is possible that these clusters do not contain any radio haloes at all, it could also just be that at the sensitivity limits of the current generation of radio telescopes (e.g. GMRT, Jansky Very Large Array) any possible weak halo emission from clusters is not detectable. However, if the hadronic model is to be believed then there will always be a component of diffuse radio emission in galaxy clusters due to relativistic protons.

For this reason, it is important to study non-detections of radio haloes just as much as detections. Using next generation telescopes like the Murchison Widefield Array (MWA; Lonsdale et al. 2009; Bowman et al. 2013; Tingay et al. 2013), LOw Frequency ARray (van Haarlem et al. 2013) and the upcoming Square Kilometer Array (Dewdney et al. 2013), which have better low surface brightness sensitivity and UV-coverage at short baselines as compared to existing telescopes, it could be possible to detect previously undetected radio haloes. The radio power in these haloes will also tell us what fraction of the power in haloes is contributed due to the hadronic model as compared to the turbulence model.

With this in mind, we decided to observe merging galaxy clusters with the MWA. These clusters were chosen from literature on the basis of their position in the sky (Southern hemisphere) as well as existing observations of the cluster and whether or not any haloes and/or relics were detected in them. Based on the above criteria, we came up with a list of nine galaxy clusters all of which are claimed to host a halo and/or a relic based on higher frequency (1.4 GHz) observations. These clusters are – Abell 13, Abell 548b, Abell 2063, Abell 2163, Abell 2254, Abell 2345, Abell 2744, PLCK G287.0+32.9 and RXC J1314.4-2515.

In Section 2, we give the details of the observations of these clusters made with the MWA as well as with the GMRT. The primary results of the paper are given in Section 3, with a discussion of these results in Section 4. The main conclusions of the paper are summarized in Section 5. The cosmology used in this paper is as follows: $\Omega_0 = 0.3$, $\Omega_\Lambda = 0.7$, $H_0 = 68$ km s^{-1} Mpc^{-1}

2 OBSERVATIONS AND ANALYSIS

2.1 GLEAM survey images

The clusters studied in this paper were observed as part of the GaLactic and Extragalactic All-sky MWA (GLEAM) Survey (Wayth et al. 2015). The survey was carried out at five frequency bands between 72 and 230 MHz, centred on 88, 118, 154, 188 and 215 MHz with 30.72 MHz bandwidth each. Each full band was further divided into four sub-bands of 7.68 MHz bandwidth. The GLEAM Survey was carried out over 2 yr. During the first year, the frequency resolution of the survey was 40 kHz while the time resolution was 0.5 s. In the second year, the frequency and time resolutions were changed to 10 kHz and 2 s, respectively. For our purposes we used the year one data.

The survey was carried out at seven declination settings ($\delta = +18\overset{\circ}{.}6, +1\overset{\circ}{.}6, -13\overset{\circ}{.}0, -26\overset{\circ}{.}7, -40\overset{\circ}{.}0, -55\overset{\circ}{.}0, -72^\circ$), utilizing a drift-scan method. At the beginning of the observation, the telescope was electronically set to one of the seven declinations and measurements were taken sequentially looping over the five frequencies every two minutes (112 s) as the sky drifted overhead. A set of calibrators were observed throughout each of the observing nights.

This raw data was then analysed and sent through a pipeline to produce the final images used in this paper. The basic steps of the analysis are as follows.

For each scan:

(i) a single bright source was used for a first-pass calibration on all the observations (Hurley-Walker et al. 2014);

(ii) cleaning of the images was performed using WSCLEAN (Offringa et al. 2014);

(iii) the primary beam model for the MWA, as described by Sutinjo et al. (2015), was used to transform to astronomical Stokes;

(iv) assuming the sky to be unpolarized, Stokes Q, U and V were set to zero and, using the same beam model, converted back to instrumental Stokes;

(v) self-calibration was now performed using this new sky model to produce the final multifrequency synthesis images.

The GLEAM images were calibrated in three steps: first, at each frequency, the model of a bright source was used to transfer the complex antenna gains to the entire drift scan data of the night. Secondly, self-calibration was performed as described earlier. Finally, bright point sources ($>8\sigma$) were chosen and cross-matched with the VLA Lowfrequency Sky Survey Redux (VLSSr) at 74 MHz, Molonglo Radio Catalogue at 408 MHz and NRAO VLA Sky Survey (NVSS) at 1400 MHz. A power law was fit to the spectra of the point sources and based on their expected to observed flux densities, a declination dependant average scaling factor was estimated at every MWA frequency and applied to the images. All the snapshots obtained during a night's observation were then combined in an inverse-noise-weighted fashion to produce mosaics at every frequency. Note that during this procedure, the absolute flux density scale of sources was set to the Baars scale (Baars et al. 1977). Details on all the above procedures can be found in Hurley-Walker et al. (2017). For most of the sources used in this paper, the uncertainties in their flux density measurements is ∼8 per cent. The images used in this paper are all taken from the GLEAM survey.

In this paper, we make use of the 30.72 MHz bandwidth images centred at 88, 118 and 154 MHz in addition to the 60 MHz bandwidth wideband image centred at 200 MHz. These wideband images were made using observations in the frequency range 170–231 MHz. These wideband images compromise between improved sensitivity and resolution and represent the best images to search for diffuse cluster emission. These wideband images have a resolution of ∼2 arcmin and an root mean square (rms) value of ∼6 mJy beam^{-1} at 200 MHz.

Estimation of rms values in the GLEAM images was carried out using the software package Background And Noise Estimation (BANE) written by Paul Hancock.[1] The standard method of estimating rms from an image would be to estimate the mean and standard deviation in a fixed size box around every pixel in the image and then average it. However, this method is extremely time consuming and will also be biased due to the presence of sources in the image.

BANE uses a slightly modified version of this algorithm to quickly and accurately estimate the rms of an image. The software works on the principle that there is a high degree of correlation between adjacent pixels in a radio image. As such, it is not necessary to estimate the mean and standard deviation in a box at every pixel. Instead, boxes are drawn around every *N*th pixel and, first, contribution from the source pixels is removed by masking pixels greater than 3σ. This sigma clipping is performed three times and then, instead of the mean, the median is estimated for each grid and interpolated to produce the background image. The same process is repeated on the background-subtracted image (data–background) and then the standard deviation of the image is estimated.

[1] https://github.com/PaulHancock/Aegean/wiki/BANE

2.2 TGSS images

The TGSS[2] is a fully observed survey of the radio sky at 150 MHz as visible from the GMRT, covering the full declination range of −55 to +90 deg. Data were recorded in half polarization (RR,LL) every 2 s in 256 frequency channels across 16 MHz of bandwidth (140–156 MHz). Each pointing was observed for about 15 min, split over three or more scans spaced out in time to improve UV-coverage. As a service to the community, this archival data has been processed with a fully automated pipeline based on the Source Peeling and Atmospheric Modelling (SPAM) package (Intema et al. 2009; Intema 2014), which includes direction-dependent calibration, modelling and imaging to suppress mainly ionospheric phase errors.

In summary, the pipeline consists of two parts: a *pre-processing* part that converts the raw data from individual observing sessions into pre-calibrated visibility data sets for all observed pointings, and a *main pipeline* part that converts pre-calibrated visibility data per pointing into stokes I continuum images. The flux density scale is set by calibration on 3C48, 3C147 and 3C286 using the models from Scaife & Heald (2012). More details on the processing pipeline and characteristics of the data products can be found in the article on the first TGSS alternative data release (ADR1; Intema et al. 2016). For this study, ADR1 images were used to create mosaics at the cluster positions. These images have a resolution of ∼25 arcsec and an rms of ∼5 mJy beam^{-1} at 150 MHz.

The primary purpose of using the TGSS images is that since they have better resolution than the GLEAM images it would be easier to detect any blending of unrelated sources that might occur with the haloes and relics. Such sources could then be identified and their flux densities subtracted in order to accurately estimate the flux densities of the haloes and relics.

3 RESULTS

In Table 1, we give the rms values of the GLEAM images used in this paper as well as those of the TGSS 150 MHz images at two separate resolutions, the original 25 arcsec images and images tapered to 60 arcsec to highlight the diffuse nature of the emission. This table also gives the resolutions of images at all the four GLEAM frequencies. Due to the poor resolution of the GLEAM images, occasionally unrelated sources get blended with the haloes and relics of interest. In order to estimate the flux densities of these haloes and relics at the GLEAM frequencies, the flux densities of the unrelated sources were subtracted. Table 2 shows the positions of these unrelated sources as well as their flux densities at 200 MHz and their spectral indices. The integrated flux densities of the haloes and relics are given in Table 3. Note here that while the TGSS measurements use the calibration scale provided by Scaife & Heald (2012) and the MWA uses the calibration scheme of Baars et al. (1977), the difference between the two scales is ∼3 per cent (Hurley-Walker et al. 2017).

We also estimated the angular sizes of the haloes and relics at 200 MHz using the task `imfit` in the Common Astronomy Software Analysis (CASA) package (Table 4). Also shown in Table 4 are the positions and linear extents of the haloes and relics as well as the redshifts of the clusters.

In Fig. 1, we show the contours of the GLEAM 200 MHz wideband images overlaid on the respective X-ray images of the clusters.

[2] TIFR (Tata Institute of Fundamental Research) GMRT Sky Survey; see http://tgss.ncra.tifr.res.in/

Table 1. Image properties for the sample of clusters with known diffuse emission studied here. Note that the TGSS beam is circular at both resolutions.

Cluster	MWA (arcsec× arcsec, °/mJy beam^{-1})				TGSS (mJy beam^{-1})	
	88 MHz	118 MHz	154 MHz	200 MHz	150 (25 arcsec)	150 (60 arcsec)
A13	287 × 263, −74	202 × 193, −76	153 × 147, −77	127 × 128, −83		
	37.7	19.3	12.7	7.8	5.0	11.4
A548b	282 × 265, 67	201 × 193, 72	153 × 148, 62	128 × 123, 39		
	38.2	16.6	12.1	6.0	4.5	9.4
A2063	324 × 383, 0	236 × 204, 4	183 × 158, 1	146 × 127, 2		
	77.9	45.3	22.2	19.6	7.1	17.0
A2163	286 × 272, 0	206 × 197, −14	158 × 150, −8	129 × 122, −10		
	62.8	36.6	20.4	14.3	3.8	8.9
A2254	347 × 278, 0	257 × 200, 0	203 × 157, 0	161 × 126, −2		
	106.9	65.9	35.7	37.6	4.4	10.9
A2345	293 × 282	203 × 198, −51	155 × 150, −45	130 × 125, −59		
	46.4	22.2	16.7	7.4	5.0	12.3
A2744	287 × 263, −56	204 × 191, −50	156 × 146, −55	129 × 122, −41		
	33.5	16.9	12.2	7.2	4.3	10.2
PLCK G287.0+32.9	278 × 264, 72	201 × 194, 73	152 × 147, 37	125 × 122, 14		
	37.9	19.7	12.2	5.6	5.0	10.2
RXC J1314.4−2515	277 × 264, 70	202 × 194, 64	152 × 149, 50	125 × 122, 61		
	42.4	24.0	15.0	8.5	5.4	10.2

Table 2. List of unrelated sources whose flux densities were subtracted from the corresponding haloes and/or relics. The flux density of the unrelated source at any given frequency is $S_\nu = S_{200}*(\nu_{\rm MHz}/200)^\alpha$. The spectral indices were estimated based on the TGSS and the higher frequency observations. Detailed references for the higher frequency observations are given in Table 3.

Cluster	Position		S_{200}	α
	RA	Dec.	(mJy)	
A13	00:13:33	−19:28:52	101.24	−2.0
A548b	05:45:21	−25:55:55	28.8	−0.74
	05:45:27	−25:55:10	4.5	0
	05:45:11	−25:54:55	22.2	−0.52
	05:45:22	−25:47:30	74.8	−0.13
A2163	16:16:03	−06:09:28	81.65	−1.59
	16:15:40	−06:13:48	373.48	−1.26
	16:15:27	−06:07:02	224.35	−1.41
	16:15:41	−06:09:08	28.46	−0.8
	16:16:23	−06:06:46	237.2	−0.65
A2345	21:27:34	−12:10:58	143.25	−0.8
	21:26:45	−12:07:29	199.22	−0.8
PLCK G287.0+32.9	11:50:43	−28:00:29	20.5	−0.6
	11:50:40	−28:01:00	14.8	−0.38
	11:50:33	−27:58:58	2.86	−0.28
	11:50:34	−28:00:05	6.85	−0.94
	11:50:50	−28:02:22	12.22	−0.6
	11:50:56	−28:01:54	20.59	−0.62
	11:51:00	−28:04:09	51.72	−0.92
	11:50:52	−28:05:24	37.01	−0.56
	11:50:46	−28:05:42	147.07	−0.9
	11:50:59	−28:00:40	34.8	−1.37
	11:50:50	−27:59:10	56.3	−0.6
	11:50:54	−27:59:10	72.2	−0.81
	11:50:59	−27:59:23	21.9	−1.44

All the X-ray images were obtained from the High Energy Astrophysics Science Archive Research Center (HEASARC) webpage[3] or the *XMM* data base.[4] We used *XMM–Newton* and *Chandra* images where available. Although we make use of the images at other MWA frequencies we are only showing the 200 MHz images as they have the best resolution and sensitivity. Fig. 2 shows the GLEAM 200 MHz image contours overlaid on the corresponding grey-scale TGSS images at 60 arcsec resolution. The exception to this is A13 for which we have used the 25 arcsec resolution image. Fig. 3 shows the spectra of all the haloes and relics that were detected.

The results on the individual clusters are discussed below.

3.1 Abell 13

A low-redshift cluster ($z = 0.0946$, Struble & Rood 1999) with a highly disturbed morphology, the X-ray distribution of Abell 13 (A13) shows two distinct clumps centred around the two brightest cluster galaxies (Juett et al. 2008). The X-ray luminosity of the cluster is $L_{\rm X[0.1–2.4\,keV]} = 1.24 \times 10^{44}$ erg s^{-1} (Piffaretti et al. 2011). A13 was observed at radio frequencies by Slee et al. (2001) where they detected an irregularly shaped relic at 1.4 GHz.

The temperature map of the cluster (Juett et al. 2008) shows a drop in the temperature at the site of the radio relic. This seems to suggest that the origin of the relic in A13 is not shock related as the temperature in regions around shock-accelerated relics is usually greater than in the cluster centres.

Fig. 1(a) shows the GLEAM 200 MHz contours of A13 overlaid on the corresponding *XMM–Newton* image. The irregularly shaped object (A) towards the west of the X-ray emission is the radio relic in A13. The other two sources – one to the N and the other to the SE of the X-ray emission – are galaxies with optical counterparts and are unrelated to the relic emission. When compared with the

[3] http://heasarc.gsfc.nasa.gov/xamin/xamin.jsp, HEASARC is a service of the Astrophysics Science Division at NASA/GSFC and the High Energy Astrophysics Division of the Smithsonian Astrophysical Observatory (SAO).
[4] http://nxsa.esac.esa.int/nxsa-web

MNRAS 467, 936–949 (2017)

Table 3. Integrated flux densities of the haloes (H) and relics (R) from this study. All the 150 MHz values are from the TGSS images. The references for the other flux densities are as follows: [a]Slee et al. (2001); [b]Feretti et al. (2006); [c]Feretti et al. (2004); [d]Feretti et al. (2001); [e]Govoni et al. (2001b); [f]Bonafede et al. (2009); [g]Bonafede et al. (2014); [h]Venturi et al. (2013); [i]Venturi et al. (2007); [j]Feretti et al. (2005). The X-ray luminosities were obtained from the MCXC meta-catalogue by Piffaretti et al. (2011). The only exception to this is PLCK G287.0+32.9 for which the X-ray luminosity was obtained from Planck Collaboration VIII (2011).

Cluster	Object	Integrated flux densities (mJy)									$L_{X[0.1-2.4keV]}$ ($\times 10^{44}$) erg s^{-1}	$\log(P_{1.4})$ W Hz^{-1}
		88 MHz	118 MHz	150 MHz	154 MHz	200 MHz	325 MHz	610 MHz	1400 MHz	3000 MHz		
A13	H	–	–	–	–	–	–	–	–	–	1.24	$\lesssim$21.79
	R	4445.5 ± 355.6	2817.4 ± 225.4	1868.1 ± 186.8	1861.9 ± 149	1290 ± 103	–	–	35.5 ± 1.7[a]	–	–	24.08
A548b	H	–	–	–	–	–	–	–	–	–	0.1	$\lesssim$21.00
	B	196.05 ± 15.68	114.51 ± 9.16	142.12 ± 14.21	168.26 ± 13.46	116.21 ± 9.3	–	–	60 ± 5[b]	–	–	23.51
	A	307.2 ± 24.6	298.4 ± 23.9	203.9 ± 20.4	256 ± 20.5	230.1 ± 18.4	–	–	61 ± 5[b]	–	–	23.51
A2063	H	–	–	–	–	–	–	–	–	–	1.14	$\lesssim$21.23
A2163	H	2828.3 ± 226.3	1178 ± 94.2	563 ± 56.3	1235.4 ± 98.8	791.1 ± 63.3	861 ± 86.1[c]	–	155 ± 2[d]	–	20.16	25.61
	R	444.4 ± 35.6	172.9 ± 13.8	89.9 ± 9	252.4 ± 20.2	132.4 ± 10.6	82 ± 8.2[c]	–	18.7 ± 0.3[d]	–	–	24.68
A2254	H	1899.8 ± 247	904.9 ± 117.6	1086.9 ± 141.3	607.8 ± 79	289.4 ± 37.6	–	–	33.7 ± 3.37[e]	–	4.79	24.79
A2345	H	–	–	–	–	–	–	–	–	–	3.9	$\lesssim$22.38
	R(E)	–	623.9 ± 49.9	555.6 ± 55.6	592.3 ± 47.4	419.8 ± 33.6	188 ± 3[f]	–	29 ± 0.4[f]	–	–	24.73
	R(W)	–	1164.2 ± 93.1	1025.1 ± 102.5	932.3 ± 74.6	747.4 ± 59.8	291 ± 4[f]	–	30 ± 0.5[f]	–	–	24.74
A2744	H	–	759.3 ± 60.7	414.9 ± 41.5	512.2 ± 41	372.5 ± 30	218 ± 21.8	–	57.1 ± 0.57[e]	–	11.82	25.73
	R	–	285.3 ± 22.8	202.9 ± 20.3	203.6 ± 16.3	129.2 ± 10.3	98 ± 10	–	18.2 ± 0.18[e]	–	–	25.24
PLCK G287.0+32.9	H	–	–	314 ± 31.4	–	–	63 ± 6[g]	26 ± 2.6[g]	–	2.9 ± 0.3[g]	17.2	25.52
	R(SE)	621.4 ± 49.7	438.3 ± 35.1	382 ± 38.2	280.7 ± 22.5	268 ± 20.2	114 ± 11.4[g]	50 ± 5[g]	25 ± 5[g]	5.2 ± 0.52[g]	–	25.72
	R(NW)	855.3 ± 224.3	683.9 ± 168.1	620 ± 62	433.2 ± 93.4	356.8 ± 68.7	216 ± 21.6[g]	110 ± 11[g]	15.2 ± 1.52[g]	–	–	25.51
RXC J1314.5−2515	H	–	–	–	–	–	40 ± 3[h]	10.3 ± 0.3[i]	–	–	9.89	24.18
	R(E)	–	96.6 ± 7.7	104.8 ± 10.5	38.1 ± 7.7	86 ± 6.9	52 ± 4[h]	28 ± 1.4[i]	11.1 ± 0.3[j]	–	–	24.71
	R(W)	–	425.3 ± 34	519.8 ± 52	267.7 ± 21.4	263.1 ± 21.1	137 ± 11[h]	64.8 ± 3.2[i]	20.2 ± 0.5[j]	–		24.97

Table 4. Haloes and relics detected by MWA. Columns 4 and 5 correspond to the peaks of emission at 200 MHz of the corresponding haloes and relics. No halo or relic was detected in A2063. The radio halo and the west relic in RXC J1314.5−2515 are blended even in the 200 MHz GLEAM image.

Cluster	Object	z	α	δ	Angular Size (arcsec × arcsec, °)			Linear size	
					θ_{maj}	θ_{min}	PA	(kpc)	(kpc)
A13	R	0.094	00:13:28	−19:29:58	150	108	36	260	180
A548b	B	0.042	05:45:22	−25:47:07	84	72	45	110	89
	A		05:44:50	−25:50:37	168	102	96	180	130
A2063	R	0.035							
A2163	H	0.203	16:15:45	−06:09:07	234	132	51	970	390
	R		16:16:10	−06:05:02	193	102	92	660	350
A2254	H	0.178	17:17:52	+19:40:37	147	109	0	450	340
A2345	R(E)	0.179	21:27:34	−12:10:41	276	78	157	710	270
	R(W)		21:26:43	−12:07:56	174	60	41	590	180
A2744	H	0.308	00:14:20	−30:23:29	192	132	63	1010	690
	R		00:14:37	−30:20:22	204	102	132	1100	400
PLCK G287.0+32.9	H	0.39	11:50:49	−28:04:36	210	150	117	900	750
	R(SE)		11:51:12	−28:11:41	252	96	77	1530	670
	R(NW)		11:50:49	−28:03:35	192	132	38	860	410
RXC J1314.5−2515	H	0.244							
	R(E)		13:14:44	−25:15:03	192	120	143	660	600
	R(W)								

1.4 GHz image of Slee et al. (2001), the relic is more extended in the GLEAM images. This extension is over and above what can be expected due to convolution effects. The apparently smaller extent of the relic emission at 1.4 GHz is due to the extended emission being resolved out in the Very Large Array-BnA configuration used by Slee et al. (2001).

In Fig. 2(a), we show the GLEAM 200 MHz contours overlaid on the corresponding 25 arcsec TGSS grey-scale image where a faint source embedded within the MWA contours is seen to the NE of the relic emission. This source is unrelated to the relic and has an optical counterpart. This source is not detected in the NVSS 1400 MHz image. We estimate the spectral index of this source to be ∼−2 based on the TGSS 150 MHz measurement and the NVSS 1400 MHz upper limit. This spectral index is consistent with the flux density estimate of this source at 74 MHz from the VLSSr images. The extrapolated flux density of this source was subtracted from the integrated flux density of source A to estimate the flux densities of the relic at all the GLEAM survey frequencies used in this study.

The spectrum of the A13 relic is shown in Fig. 3(a). No diffuse radio emission (halo) associated with the cluster X-ray emission was detected. Slee et al. (2001) produced a spectrum for the relic over the frequency range 80–1400 MHz which showed a curvature that is not seen by our measurements. However, it should be mentioned that the curved spectrum of the A13 relic as seen by Slee et al. (2001) is largely influenced by the Culgoora flux density measurements at 80 MHz. Given the uncertainty in the Culgoora measurements we do not believe that the A13 relic has a curved spectrum. With the currently available more accurate flux density measurements of the relic using MWA we believe the relic spectrum to fit a power law and not the curved spectrum as seen by Slee et al. (2001).

3.2 Abell 548b

Abell 548b (A548b) is a dynamically unrelaxed cluster at a redshift of $z = 0.0424$ (den Hartog & Katgert 1996) but is not extremely X-ray luminous ($L_{X[0.1–2.4\,keV]} = 0.1 \times 10^{44}$ erg s^{-1}, Piffaretti et al. 2011).

The cluster is claimed to contain two radio relics: one to the north and the other to the north-west of the cluster centre. The NW relic was first detected by Giovannini et al. (1999) and later confirmed through more detailed observations by Feretti et al. (2006). These two claimed relics are ∼500 kpc from the cluster centre and near the boundary of the X-ray emission (Solovyeva et al. 2008).

In addition to the above two relics, Feretti et al. (2006) also detected diffuse emission from an irregular source closer to the centre of the cluster. While not entirely certain of its nature, they posit that this source could be the result of an internal shock in the cluster whereas the other two relics are believed to trace the outgoing shocks generated at the time of cluster merger.

Fig. 1(b) shows the GLEAM 200 MHz contours overlaid on the *XMM* X-ray image of this cluster. There are four sources of interest that we have labelled A, B, C and D in the figure. While the source D is a known radio galaxy with an optical counterpart (PGC17721), the nature of the sources A and B, that are claimed to be cluster relics (Feretti et al. 2012) is still a mystery. We discuss this in detail in a later section of the paper. The central diffuse source (C), near the northern edge of the X-ray emission, is a complex source. High-resolution images of this source (Feretti et al. 2006) reveal that source C is in fact a combination of three objects – the outer two of which are compact objects even in the Australia Telescope Compact Array 2.5 GHz images. The central object, however, is diffuse in nature and has no optical source associated with it. We estimate the spectral index of this diffuse source between 118 MHz and 1.4 GHz to be -0.7 ± 0.1. Based on its radio morphology (Feretti et al. 2006) and spectral index, this source appears to be a radio galaxy. No diffuse radio emission (halo) associated with the X-ray distribution was detected in this cluster.

In Fig. 2(b), we have overlaid the GLEAM 200 MHz contours on the corresponding 60 arcsec TGSS image.

3.3 Abell 2063

Abell 2063 (A2063) is a low-redshift ($z = 0.0343$, Hill & Oegerle 1993) galaxy cluster with an X-ray luminosity of $L_{X[0.1–2.4\,keV]} = 1.14 \times 10^{44}$ erg s^{-1} (Reiprich & Böhringer 2002).

The GLEAM 200 MHz contours for A2063 are overlaid on the *Chandra* X-ray emission in Fig. 1(c). In Fig. 2(c), the 200 MHz

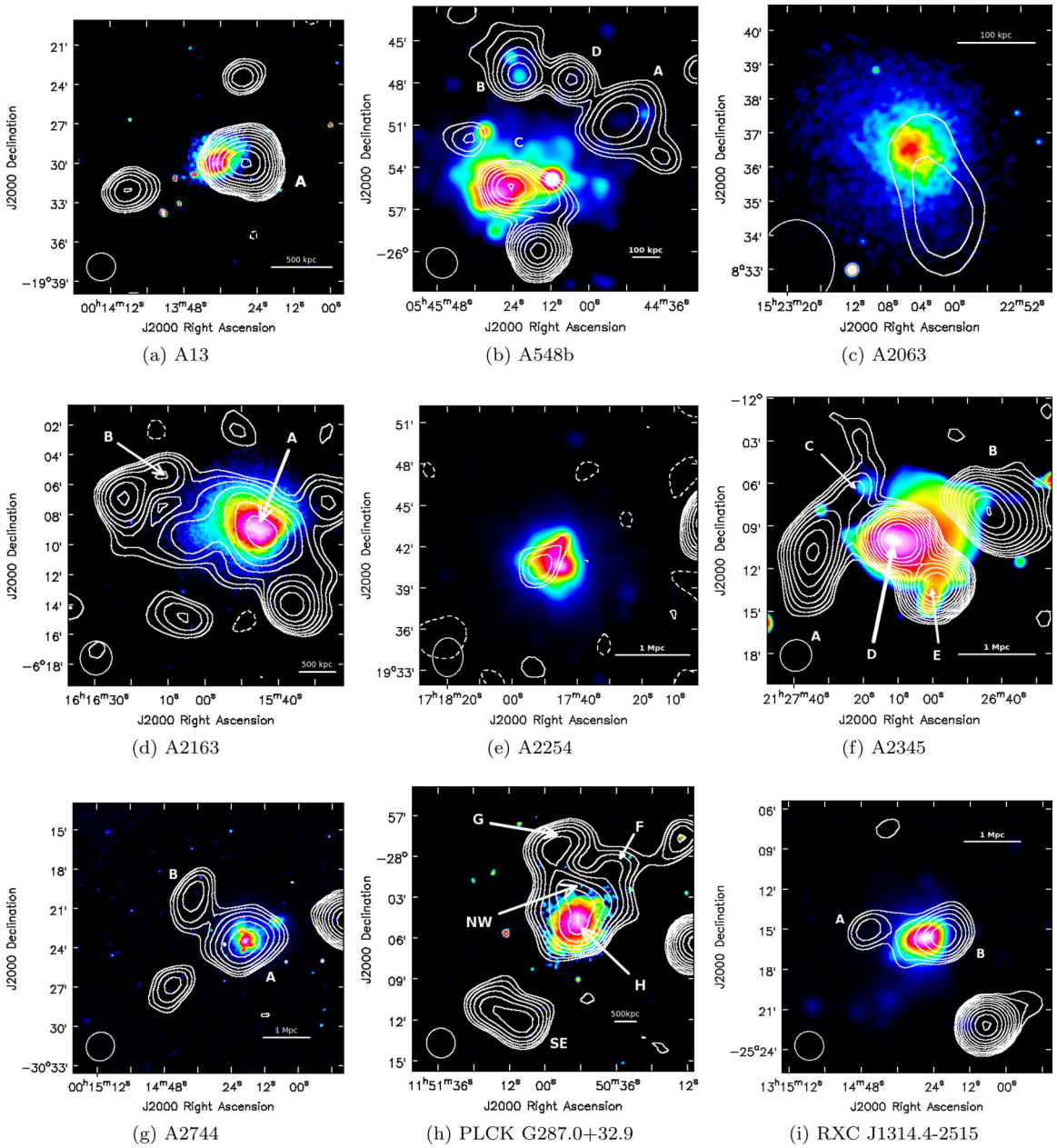

Figure 1. GLEAM 200 MHz contours (60 MHz bandwidth) overlaid on the respective X-ray images of the clusters. The contours start at 3σ (at 2σ for A2254) and increase by $\sqrt{2}$ thereafter. See Table 1 for σ values. The first negative contour at 3σ (at 2σ for A2254) is also plotted (dashed lines). The full width half-maximum of the synthesized beam of the MWA is indicated in the bottom left corner.

contours are overlaid on the corresponding TGSS image. The TGSS radio source, which is unresolved at 25 arcsec resolution, has an optical counterpart with a redshift corresponding to that of the galaxy cluster and is most likely a galaxy.

The radio emission shown in Fig. 1(c) is due to a combination of this head–tail radio galaxy and another radio galaxy co-located with the X-ray emission. The latter source, [OL97]1520+087, has been discussed in Kanov, Sarazin & Hicks (2006). No diffuse emission in the form of relics or haloes were detected in this cluster. The claimed relic in this cluster (Feretti et al. 2012) is the source 3C318.1 which is 2.4 Mpc from the cluster centre and is a relic radio galaxy. This source is discussed in detail by Komissarov & Gubanov (1994) and is not relevant to the present discussion.

3.4 Abell 2163

Abell 2163 (A2163; $z = 0.203$, Struble & Rood 1999) is one of the hottest and most X-ray luminous clusters known ($L_{\mathrm{X[0.1–2.4\,keV]}} = 20.16 \times 10^{44}$ erg s^{-1}, Piffaretti et al. 2011). The X-ray distribution of the cluster shows two primary sub-clusters – one to the west and a secondary one to the north (Bourdin et al. 2011). The primary sub-cluster of A2163 (west) shows a bullet-like nature suggesting a recent merger in the E-W direction. The north sub-cluster appears to have not had any recent interaction with the west sub-cluster and is well separated from it.

This cluster contains a giant radio halo ($l \sim 3$ Mpc) in the middle and a small radio relic north-east of the cluster centre (Feretti et al. 2001).

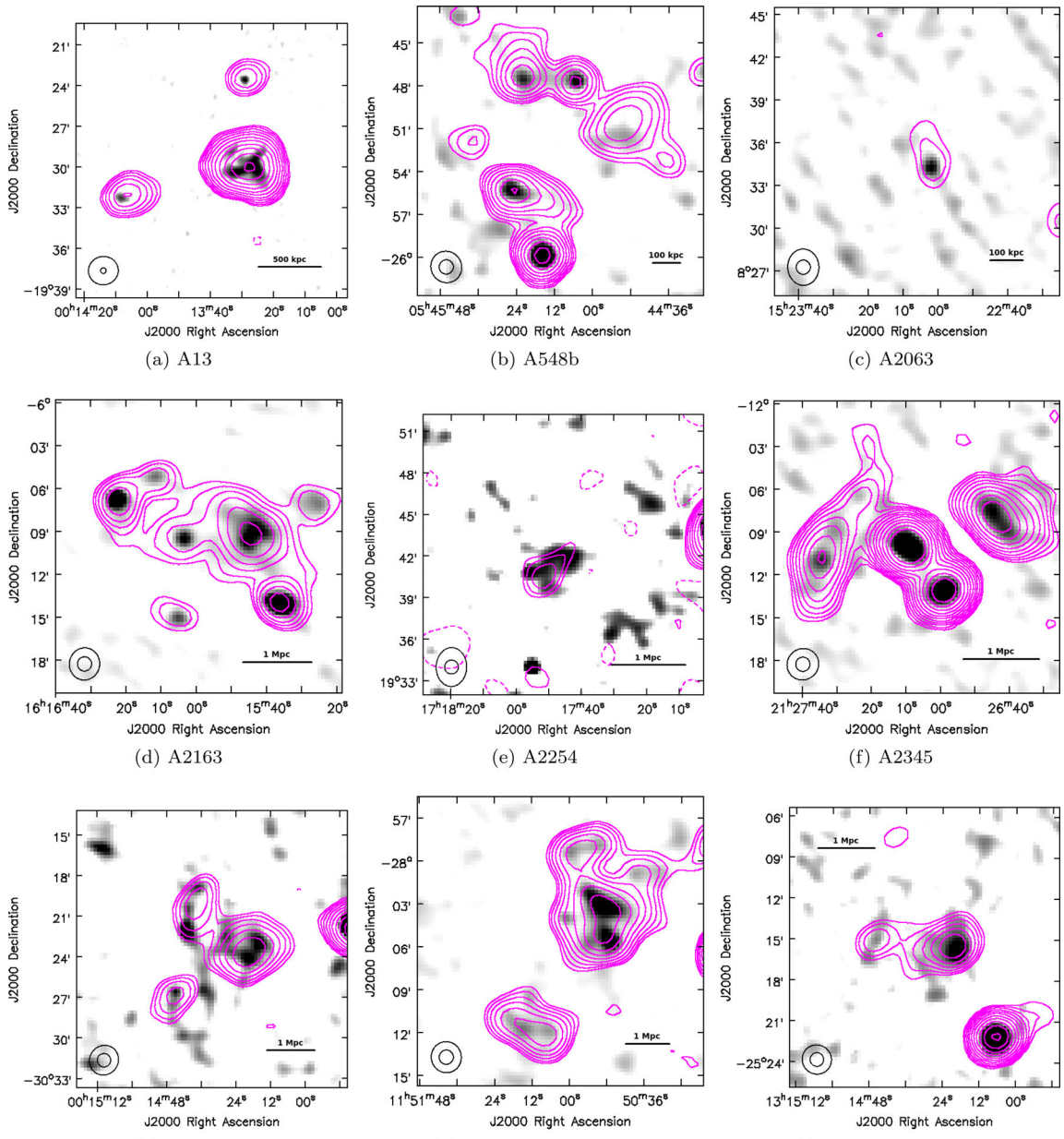

(a) A13 (b) A548b (c) A2063

(d) A2163 (e) A2254 (f) A2345

(g) A2744 (h) PLCK G287.0+32.9 (i) RXC J1314.4-2515

Figure 2. GLEAM 200 MHz (60 MHz bandwidth) contours overlaid on the corresponding grey-scale TGSS 150 MHz images. All the TGSS images are at 60 arcsec resolution except for A13 which is at 25 arcsec resolution. Contours start at 3σ (at 2σ for A2254) and increase by $\sqrt{2}$ thereafter. The first negative contour at 3σ (at 2σ for A2254) is also plotted (dashed lines). The full width at half-maxima of the synthesized beams of the GLEAM and TGSS images are indicated in the bottom left corner.

Figs 1(d) and 2(d) show the GLEAM 200 MHz contours of this cluster overlaid on the corresponding *XMM–Newton* X-ray image and the TGSS image, respectively. The central radio halo (A) and the relic (B) are detected in all the GLEAM images (see Table 3 for their flux densities). These flux densities were estimated after subtracting the flux densities of unrelated sources (Fig. 2d). The flux densities of these unrelated sources estimated at 150 MHz (TGSS images) and at 1400 MHz (Feretti et al. 2001) were used to estimate their spectra and their flux densities at all the GLEAM survey frequencies given in Table 3.

3.5 Abell 2254

The galaxy cluster Abell 2254 (A2254) is a rich, X-ray luminous cluster ($L_{\mathrm{X[0.1–2.4\,keV]}} = 4.79 \times 10^{44}$ erg s^{-1}, Böhringer et al. 2000) located at a redshift of $z = 0.178$ (Crawford et al. 1995).

Optical and X-ray analysis of the cluster (Girardi et al. 2011) suggest that A2254 is a highly disturbed cluster with a very complex morphology. There are two major clumps of galaxies separated by $\sim 0.5\,h_{70}^{-1}$ Mpc in the east–west direction. While the primary X-ray peak coincides with the Brightest Cluster Galaxy (BCG), the secondary X-ray peak in the east clump does not, suggesting that the cluster is still in the middle of an ongoing merger.

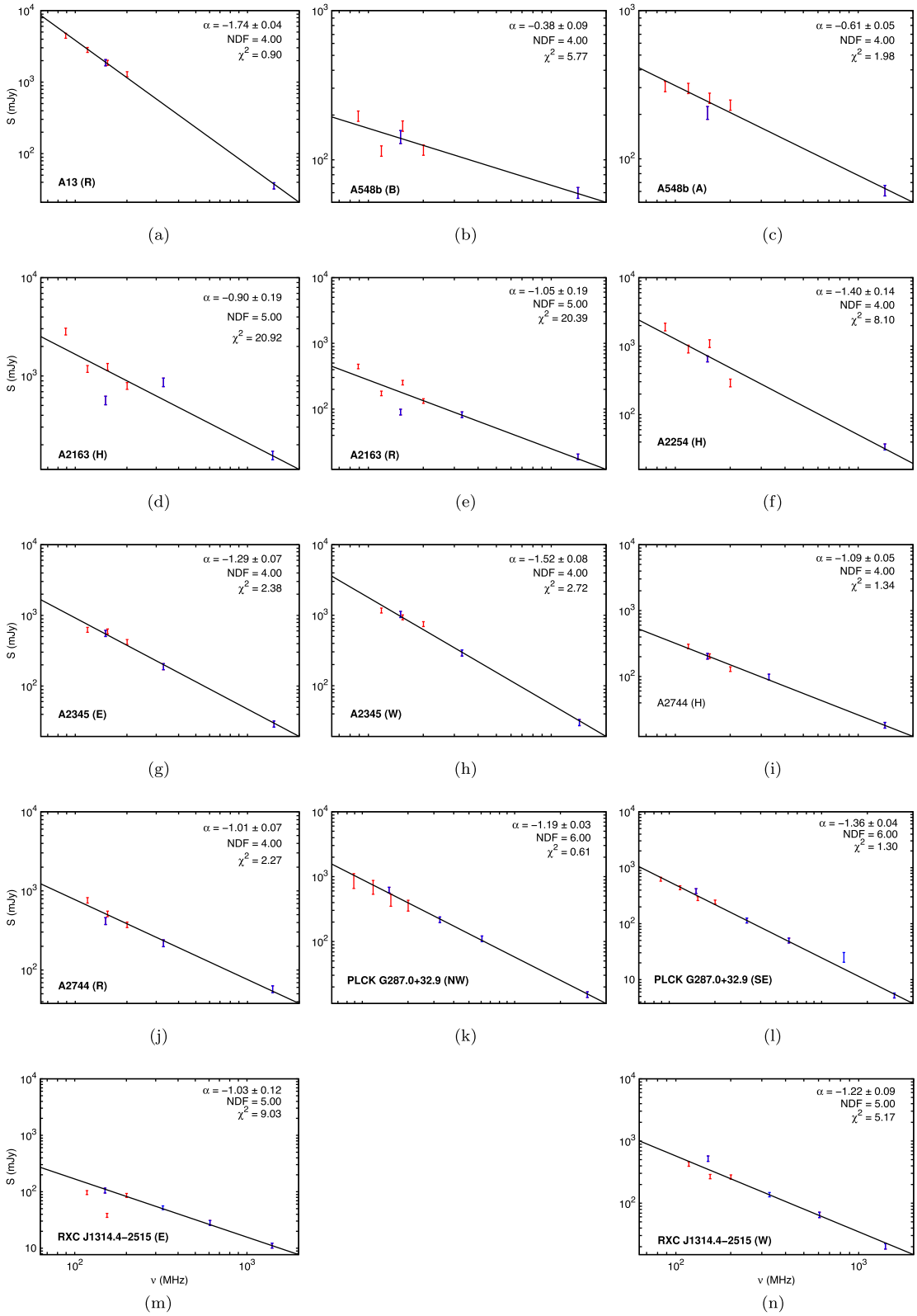

Figure 3. Spectra of haloes and relics. Data points in red colour are from the GLEAM survey measurements while those in blue colour are measurements from other telescopes. Note that the range of frequencies along the *x*-axis is identical in all the panels and is specified in the bottom-most panel. Every panel also shows the spectral index value (α), the number of degrees of freedom (NDF) and the reduced χ^2 value of the fit.

Radio observations of A2254 (Govoni et al. 2001b) show an irregularly shaped radio halo with clumpy features. Fig. 1(e) shows the GLEAM 200 MHz contours overlaid on the corresponding *XMM* X-ray image. The halo is seen at all the available GLEAM images.

We show the same 200 MHz contours overlaid on the corresponding 60 arcsec TGSS image in Fig. 2(e). Note that the rms value in the 200 MHz image of A2254 is ∼37 mJy beam^{-1} which is ∼5 times larger when compared with the rms values in the other 200 MHz images. This is because of the position of this cluster. At a declination of ∼+20d, A2254 is at the northern-most declination setting for MWA which results in a larger synthesized beam and rms.

3.6 Abell 2345

Abell 2345 (A2345) is a highly disturbed, X-ray luminous ($L_{\rm X[0.1–2.4\,keV]} = 3.9 \times 10^{44}$ erg s^{-1}, Böhringer et al. 2004) galaxy cluster. The redshift of the cluster is found to be $z = 0.1789$ (Boschin, Barrena & Girardi 2010).

Boschin et al. (2010) also highlighted the complex sub-structure in the cluster. A2345 contains three distinct sub-clumps as seen in optical and X-ray. These clumps lie in the east, south-east and north-west directions.

Extended diffuse emission from A2345 was first seen by Giovannini et al. (1999) as part of the NVSS and later confirmed through detailed observations at 325 MHz and 1.4 GHz by Bonafede et al. (2009). The cluster contains two relics (A and B) on opposite sides of the cluster centre, both ∼1 Mpc from the cluster centre. Each relic is about 1 Mpc in size.

In Fig. 1(f), we show the GLEAM 200 MHz contours overlaid on the corresponding *XMM* X-ray image. The two relics are seen to the east (A) and to the west (B) of the central X-ray emission. The source above the east relic (C), which has a counterpart in the 60 arcsec TGSS image (Fig. 2f), is an unresolved source, has an infrared counterpart in the Two Micron All Sky Survey images and is unrelated to the relic emission. The source D is a cD galaxy while the source E is another radio galaxy in the cluster (Bonafede et al. 2009). The image obtained after subtracting sources D and E does not detect any radio halo that is associated with the cluster. Table 3 contains the flux densities for the relics at all the GLEAM frequencies except 88 MHz where they get blended with other sources.

3.7 Abell 2744

The cluster Abell 2744 (A2744) is located at a redshift of $z = 0.308$ (Struble & Rood 1999) and is extremely luminous in X-ray ($L_{\rm X[0.1–2.4\,keV]} = 11.82 \times 10^{44}$ erg s^{-1}, Ebeling et al. 2010).

Optical and X-ray analysis of this cluster (Kempner & David 2004; Boschin et al. 2006; Owers et al. 2011) shows that it is currently undergoing a merger in the north–south direction.

A giant radio halo (∼2.4 Mpc) was first seen in the cluster by Govoni et al. (2001a,b). In addition to the halo, this cluster also contains an elongated radio relic north-east of the cluster centre.

The radio halo and the relic were detected in the GLEAM survey at all the observed frequencies (Table 3). The flux densities of the halo and relic at 88 MHz are not given as they get blended with each other at that frequency. Fig. 1(g) shows the GLEAM 200 MHz contours overlaid on the *XMM* X-ray image. The contours of the radio halo (A) are aligned with the X-ray emission. The radio relic (B) is the source NE of the X-ray and halo emission. The source SE of the X-ray distribution has an optical counterpart and is unrelated to the halo and relic emission. The GLEAM 200 MHz contours are overlaid on the corresponding 60 arcsec TGSS image in Fig. 2(g).

3.8 PLCK G287.0+32.9

PLCK G287.0+32.9 is a high redshift ($z = 0.39$), highly X-ray luminous ($L_{\rm X[0.1–2.4\,keV]} = 17.2 \times 10^{44}$ erg s^{-1}, Planck Collaboration VIII 2011) galaxy cluster which contains radio relics (Bagchi et al. 2011) on opposite sides of the cluster centre to the north and south.

Subsequent observations of the cluster (Bonafede et al. 2014) revealed that the source identified by Bagchi et al. (2011) as the north relic was in fact the lobe emission from a galaxy. The true north relic was located south-west of this emission. The projected separation between the relics was estimated to be ∼3.2 Mpc which is one of the largest known separations between double relics. The cluster also contains a radio halo near the cluster centre (Bonafede et al. 2014).

In Fig. 1(h), we show the GLEAM 200 MHz contours overlaid on the corresponding *XMM–Newton* image. The south-east relic (SE), the north-west relic (NW) and the halo (H) are marked in the figure. Also shown are the galaxy (G) and the region further to the north-west (F) which get blended with the north-west relic and halo at frequencies below 200 MHz. GMRT observations of the cluster by Bonafede et al. (2014) at 150 (50 arcsec), 325 (13 arcsec) and 610 MHz (7 arcsec) show the presence of 10 unresolved sources near the halo and north-west relic region. In order to estimate the flux density of the north-west relic, we first had to subtract the flux densities of all these unrelated sources. The flux densities of these unrelated sources at GMRT frequencies are available in Bonafede et al. (2014) and the extrapolated flux densities at MWA frequencies were subtracted from the total flux density in this region. Subtracting all the unrelated sources still leaves the halo and the north-west relic blended. We extrapolated the halo flux density to the MWA frequencies using the flux density values given in (Bonafede et al. 2014, Table 3) and subtracted it from the remaining flux density. This is quoted as the flux density of the north-west relic in Table 3.

Fig. 2(h) shows the GLEAM 200 MHz contours overlaid on the corresponding 60 arcsec TGSS 150 MHz image. Note that the TGSS image also detects the radio halo.

In Figs 3(k) and (l), we plot the spectra for the north-west and the south-east relic, respectively.

3.9 RXC J1314.4−2515

A highly X-ray luminous cluster ($L_{\rm X[0.1–2.4\,keV]} = 9.89 \times 10^{44}$ erg s^{-1}, Piffaretti et al. 2011), RXC J1314.4−2515 is at a redshift of $z = 0.247$ (Valtchanov et al. 2002). The X-ray emission is distorted in the NW–SE direction and is not centred on the two BCGs in the cluster (Valtchanov et al. 2002).

Radio observations of the cluster (Feretti et al. 2005; Venturi et al. 2007) reveal the presence of two radio relics – one to the east and another to the west of the cluster and a radio halo in the middle with a bridge to the west relic.

Fig. 1(i) shows the GLEAM 200 MHz contours of the cluster overlaid on the corresponding *XMM* X-ray image. The contours of the east relic (A) are seen towards the edge of the X-ray emission. The source seen to the west of the X-ray emission (B) is a convolution of the west relic and the radio halo in the cluster. Even at 200 MHz, it is not possible to separate the halo emission from that of the west relic. Estimating the flux density of the east relic was straightforward. In order to estimate the flux density of the west relic, we first extrapolated the flux density of the halo at 610 MHz (Venturi et al. 2007) to the MWA frequencies (up to 118 MHz) by

assuming a spectral index of −1.34. This spectral index of −1.34 is the average spectral index of haloes from literature (Feretti et al. 2012). This extrapolated halo flux density was subtracted from the total flux density of the region B in order to get the flux density of the west relic. At 88 MHz, however, the east relic gets blended with the west relic and the halo and hence their flux densities are not estimated at 88 MHz (Table 3).

In Fig. 2(i), we show the contours of the GLEAM 200 MHz image overlaid on the corresponding 60 arcsec TGSS image.

4 DISCUSSION

Combining the GLEAM and TGSS flux density measurements along with all available measurements in literature (see Table 3), we estimated the spectral indices of the detected haloes and relics in the range 80–1400 MHz. In the case of PLCK G287.0+32.9, however, the spectrum is estimated over the range 80–3000 MHz. In Fig. 3, we have shown the spectra of the radio haloes and relics in the nine clusters we observed. The spectra follow a power law over the frequency range 80–1400(/3000) MHz with no breaks. The mean values are $\alpha = -1.13 \pm 0.21$ for haloes and $\alpha = -1.2 \pm 0.19$ for relics. These mean values are in agreement, within errors, with the mean values of spectral indices in literature for haloes ($\alpha = -1.34 \pm 0.28$) and relics ($\alpha = -1.42 \pm 0.37$) (Feretti et al. 2012). Most of the spectral index estimates of haloes and relics in literature are in the range 325–1400 MHz, while in this study the estimates are in the range 80–1400 or 80–3000 MHz.

There are two exceptions to this result in our sample of clusters. The first is A548b whose relics have flat spectral indices [−0.61 (A) and −0.38 (B)] and the other is A13 where the relic has a steeper spectral index of −1.74.

The steep spectrum of the A13 relic can be attributed to the fact that it is not a typical shock accelerated relic. X-ray analysis using *Chandra* (Juett et al. 2008) shows that while the cluster is undergoing a merger event there are no shocks near the position of the radio relic. Moreover, the 1.4 GHz image of A13 shows this relic radio emission trailing from the brightest cluster galaxy located at the peak of the X-ray emission. The above authors suggest that this galaxy could have hosted an AGN in the past and the relic is a remnant of that emission. They propose two scenarios to explain this: either the radio plasma rose buoyantly to its current position, or the galaxy moved away during the merger event leaving behind the radio plasma that is now seen as a relic. In either scenario, there is no influx of new high-energy electrons to this relic as the AGN is not active any more. As a result, the radio spectrum of this relic emission is steeper than the mean spectra of cluster relics which are produced by cluster merger shocks. This source is a relic radio galaxy rather than a cluster relic.

In the case of A548b, it is debatable if the sources A and B are truly radio relics driven by merger shocks of the cluster or merely the lobes of radio emission produced by one or more of the cluster galaxies detected in the vicinity of these sources, including the source D (Fig. 1).

It is possible to consider the sources A and B as relics in the cluster produced by merger shocks. There is some evidence supporting this scenario because the temperature distribution of the cluster shows a jump near the positions of the sources A and B (Solovyeva et al. 2008). However, as has been discussed in this paper, the relics are towards the outskirts of the cluster and are located in a region of poor signal-to-noise ratio in the X-ray images. Therefore, the evidence for the temperature jump near the relics is rather marginal. Furthermore, the radio morphologies of the relics observed in the higher frequency images (Feretti et al. 2006) do not show any sharp boundaries usually observed in other cluster relics, but, are rather diffuse and irregular, resembling more like the radio emission or, the relict radio emission produced by radio galaxies and/or quasars.

It appears more likely that the sources A and B are lobes created by one or more of the cluster galaxies. In the case of source B, there is a small angular diameter (4 arcsec × 2 arcsec) cluster radio source (ESO 488−G006) with a flat spectral index embedded in this diffuse emission (Feretti et al. 2006). In the case of source A, there are two cluster galaxies (source D and the extension seen towards south-west of source A in Fig. 1) within ∼100 kpc of this diffuse radio emission either of which could be responsible for this diffuse radio emission.

It appears that the sources A and B are more likely to be lobes of radio galaxies rather than cluster relics.

Fig. 4 shows the empirical relation (L_X–$P_{1.4}$) between the radio power of the halo at 1.4 GHz ($P_{1.4}$) and the total X-ray luminosity of the cluster (L_X) in the range 0.1–2.4 keV. Based on the GMRT Radio Halo Survey, Brunetti et al. (2007, 2009) estimated upper limits to the halo emission in clusters where none were detected. The upper limits plotted in Fig. 4 (black crosses; Venturi et al. 2007, 2008; Kale et al. 2013) correspond to clusters in the redshift range $z = 0.2$–0.4 and to an assumed halo size of 1 Mpc. These upper limits appear to correspond to *off-state* clusters compared to the detections which are in an *on-state*. It has been known that, for the most part, *on-state* clusters are the more disturbed clusters while the *off-state* clusters are relaxed. However, if the *hadronic* model is to be believed, there should be some amount of relativistic electrons in the ICM in either case.

Five of the nine clusters studied in this paper contain radio haloes which were detected by MWA. These clusters are shown in Fig. 4 with red squares. No radio haloes were detected in the remaining four clusters – A13, A548b, A2063 and A2345. Based on the rms values in the respective images at 200 MHz, we have been able to put upper limits on the radio powers of any possible radio haloes that might be present in these clusters. These rms values were estimated after removing the already known non-halo sources in the GLEAM 200 MHz images using BANE (see Section 2.1) and then estimating the rms values from the central regions of the clusters in the residual images. The rms values thus estimated correspond to radio powers of haloes whose linear extents are comparable to those of the spatial resolutions in these images. The linear sizes corresponding to the spatial resolutions in these four images are given in column 4 of Table 5. The upper limits shown in Fig. 4 (red crosses) correspond to radio powers of such haloes. However, note that these upper limits at 1.4 GHz were obtained after extrapolating the respective values at 200 MHz with a spectral index of −1.34 which is the mean value of the spectral indices of haloes (Feretti et al. 2012). If the haloes in the current sample have spectra which are steeper than the mean value then the limits would be lower than those estimated here. The upper limit to the radio power of halo emission from A548b is consistent with that expected from the empirical L_X–$P_{1.4}$ relation (best-fitting line shown in Fig. 4). Note that this best-fitting line (Brunetti et al. 2009) corresponds to Giant Radio Haloes with linear extent, $l \gtrsim 1$ Mpc. We discuss the upper limits on the remaining three clusters below.

The upper limits on the radio powers of haloes at 1.4 GHz in A13, A2063 and A2345 (shown in Fig. 4) are factors of ∼30, 120 and 90 below that expected from the L_X–$P_{1.4}$ relation, respectively. If the extents of the radio haloes in these clusters are ∼ Mpc (canonical halo size) the upper limit obtained for A2063 is consistent with the L_X–$P_{1.4}$ relation. However, the upper limits obtained for A13 and

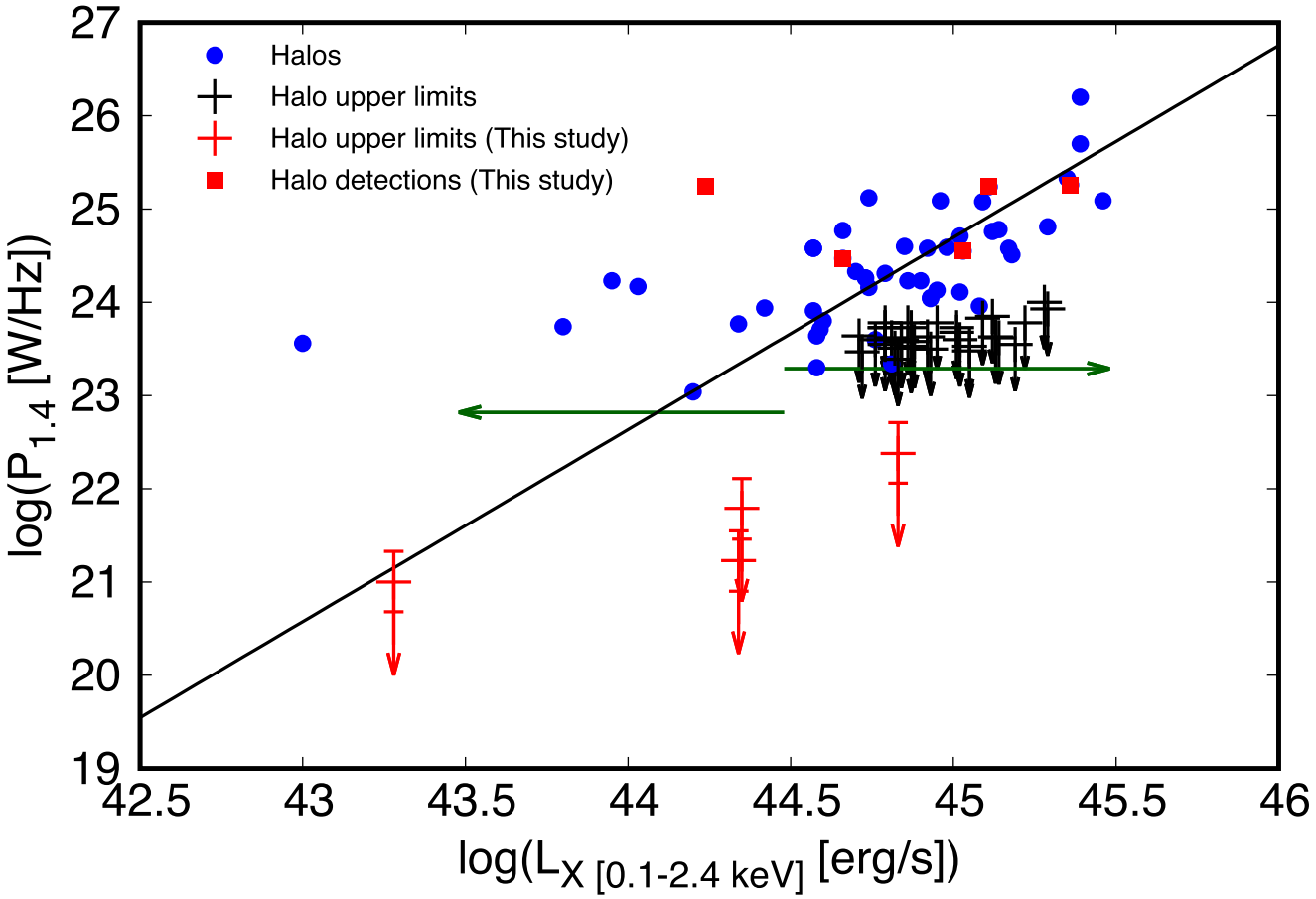

Figure 4. Plot showing the relation between the $L_{X[0.1\text{-}2.4keV]}$ of a cluster and the radio power at 1.4 GHz ($P_{1.4}$) of the halo in the cluster. The filled blue circles represent all the known radio haloes (Feretti et al. 2012). The solid black line is the best fit to the L_X–$P_{1.4}$ relation for radio haloes (Brunetti et al. 2009). The black arrows represent the upper limits to halo emission (Venturi et al. 2007, 2008; Kale et al. 2013). The MWA halo detections are shown as red squares while the upper limits are shown as red arrows. Note that the MWA upper limits were estimated using the rms values estimated in the respective images at 200 MHz and then extrapolating to 1.4 GHz with a spectral index of −1.34. The four MWA upper limits, from left to right, are – A548b, A2063, A13 and A2345. The five MWA halo detections, from left to right, are – PLCK G287.0+32.9, A2254, RXC J1314.4−2515, A2744 and A2163. The green arrows show the upper limits to the radio powers in the *off-state* radio haloes based on their X-ray luminosities as given by Brown et al. (2011).

Table 5. Upper limit clusters. The linear extents corresponding to the resolutions are given.

Cluster	rms (mJy beam^{-1})	Resolution (arcsec)	Linear extent (kpc)
A13	9.2	133	240
A548b	7.8	132	120
A2063	19.2	121	88
A2345	9.2	136	420

A2345 are lower than the expected values by a factor of ∼2 and 20, respectively.

Estimates of the upper limits on the radio powers of haloes in galaxy clusters have been carried out before. Brown et al. (2011) used the radio continuum images of galaxy clusters from the Sydney University Molonglo Sky Survey (Bock, Large & Sadler 1999) in order to estimate such constraints. By stacking 105 clusters based on their X-ray luminosities, they found that for high X-ray luminosity ($L_X > 3 \times 10^{44}$ erg s^{-1}) clusters, the upper limit on the average radio power is $(1.95 \pm 0.75) \times 10^{23}$ W Hz^{-1}, whereas for the low-luminosity ($L_X < 3 \times 10^{44}$ erg s^{-1}) clusters, the upper limit on the average radio power is $(0.66 \pm 0.89) \times 10^{23}$ W Hz^{-1}. The green arrows in Fig. 4 show the upper limits for both low and high X-ray luminosity clusters. The individual upper limits obtained in this study with the MWA observations are comparable to, or, better than the average limits obtained by Brown et al. (2011).

It is instructive to discuss the upper limits on the radio powers of haloes in many clusters in the context of the hadronic, or, secondary model. In order to estimate the contribution of the secondary model to radio emission from haloes, it is necessary to first estimate the contribution of high-energy cosmic ray (CR) protons to the energy content of the cluster. Brunetti et al. (2008) show (fig. 3 in their paper) how the ratio of the relativistic protons to the thermal protons (ϵ_p/ϵ_{th}) varies as a function of the magnetic field (B) in the cluster. This relation depends on the spectral index (δ) of the proton distribution [$N(p) \propto p^{-\delta}$, where p is the particle momentum] as well as the temperature (T) and the number density of thermal protons (n_{th}) in the cluster. Assuming n_{th} in the system to be ∼1500 m^{-3} and the proton spectral index $\delta = 2.5$, fig. 3 in Brunetti et al. (2008) shows how the energy density of CR protons varies as a function of its magnetic field. Increasing the magnetic field from 0.5 to 5 μG (Bonafede et al. 2010) decreases the energy content of the cluster due to the CR proton component from 10 per cent to 0.25 per cent. Furthermore, Brunetti & Blasi (2005) show that for a given

magnetic field, the efficiency of electron acceleration decreases with increasing values of both $n_{\rm th}$ as well as $\epsilon_{\rm p}/\epsilon_{\rm th}$, due to the increased damping of Alfvén waves on the protons.

Recent analysis of the Coma cluster (Brunetti & Lazarian 2011) suggests that the strength of synchrotron emission due to the hadronic model is a factor of 10 smaller as compared to the primary model. The upper limits on the radio powers of haloes in A13 and A2345 are ∼10 times below the expected value. However, the upper limit on the radio power of a halo in A2063 is more than 50 times smaller than that expected. It should be noted, however, that the number of unknowns in these systems is still quite large. While the electron density ($n_{\rm e}$), and hence the proton density ($n_{\rm p}$) in the clusters are known, the magnetic field, B, and the CR proton energy content, $\epsilon_{\rm p}/\epsilon_{\rm th}$, are still unknown. The cluster A2063, being a relaxed cluster could well host a weak magnetic field (<1 μG) resulting in a much weaker emission from the hadronic model. Independent measurements of magnetic fields in these clusters is crucial to the verification of the hadronic models.

5 SUMMARY

In this paper, we have presented low-frequency observations of nine merging galaxy clusters using the MWA. These observations were carried out at five frequencies (88, 118, 154, 188 and 215 MHz) as part of the GLEAM survey. The images were products of a standard pipeline developed to analyse all of the GLEAM survey data. Furthermore, better resolution (∼60 arcsec) TGSS 150 MHz images were used to compare with the corresponding MWA images in order to identify and subtract unrelated sources that are blended with the halo and relic emission.

We have detected radio relics in seven of the nine clusters and also estimated their spectra over the frequency range 80–1400 MHz (or, in the case of PLCK G287.0+32.9, 80–3000 MHz). These spectra were found to be fit by a power law over this range. The cluster A548b was found to contain radio sources (which were claimed to be relics) with the flattest spectral indices in the current sample (-0.38 and -0.61). Based on this study, we believe these sources to be radio lobes rather than relics produced in merger shocks. The relic in A13 was found to have the steepest spectrum in the current sample ($\alpha = -1.74$). However, the origin of this relic is not due to merger-driven shocks but rather it is the remnant emission from an old radio galaxy.

In five of the nine clusters, we detected the radio haloes that were first seen in high-frequency (∼1.4 GHz) observations. Their spectra fit a power law with no breaks in the range 80–1400 MHz. In the remaining four clusters where no radio haloes were detected, we have placed upper limits to their radio powers. These upper limits are a factor of 2–20 below that expected from an empirical relation between the X-ray luminosities of clusters and the radio powers of haloes in the corresponding clusters. Lack of independent measurements of magnetic fields in these clusters precludes one from putting serious constraints on the hadronic model at this stage.

ACKNOWLEDGEMENTS

We thank the referee for detailed and critical comments. This scientific work makes use of the Murchison Radio-astronomy Observatory, operated by Commonwealth Scientific and Industrial Research Organisation. We acknowledge the Wajarri Yamatji people as the traditional owners of the Observatory site. Support for the operation of the MWA is provided by the Australian Government (National Collaborative Research Infrastructure Strategy), under a contract to Curtin University administered by Astronomy Australia Limited. We acknowledge the Pawsey Supercomputing Centre that is supported by the Western Australian and Australian Governments. Parts of this research were conducted by the Australian Research Council Centre of Excellence for All-sky Astrophysics (CAASTRO), through project number CE110001020. MJ-H, QZ and LH were supported in this work by grants to MJ-H from the Marsden Fund and the New Zealand Ministry of Business, Innovation and Employment.

REFERENCES

Ackermann M. et al., 2010, ApJ, 717, L71
Aharonian F. et al., 2009a, A&A, 495, 27
Aharonian F. et al., 2009b, A&A, 502, 437
Aleksić J. et al., 2010, ApJ, 710, 634
Baars J. W. M., Genzel R., Pauliny-Toth I. I. K., Witzel A., 1977, A&A, 61, 99
Bacchi M., Feretti L., Giovannini G., Govoni F., 2003, A&A, 400, 465
Bagchi J. et al., 2011, ApJ, 736, L8
Blandford R., Eichler D., 1987, Phys. Rep., 154, 1
Blasi P., Colafrancesco S., 1999, Astropart. Phys., 12, 169
Bock D. C.-J., Large M. I., Sadler E. M., 1999, AJ, 117, 1578
Böhringer H. et al., 2000, ApJS, 129, 435
Böhringer H. et al., 2004, A&A, 425, 367
Bonafede A., Giovannini G., Feretti L., Govoni F., Murgia M., 2009, A&A, 494, 429
Bonafede A., Feretti L., Murgia M., Govoni F., Giovannini G., Dallacasa D., Dolag K., Taylor G. B., 2010, A&A, 513, A30
Bonafede A., Intema H. T., Brüggen M., Girardi M., Nonino M., Kantharia N., van Weeren R. J., Röttgering H. J. A., 2014, ApJ, 785, 1
Boschin W., Girardi M., Spolaor M., Barrena R., 2006, A&A, 449, 461
Boschin W., Barrena R., Girardi M., 2010, A&A, 521, A78
Bourdin H. et al., 2011, A&A, 527, A21
Bowman J. D. et al., 2013, PASA, 30, 31
Brown S., Emerick A., Rudnick L., Brunetti G., 2011, ApJ, 740, L28
Brunetti G., Blasi P., 2005, MNRAS, 363, 1173
Brunetti G., Jones T. W., 2014, Int. J. Mod. Phys. D, 23, 30007
Brunetti G., Lazarian A., 2011, MNRAS, 410, 127
Brunetti G., Setti G., Feretti L., Giovannini G., 2001, MNRAS, 320, 365
Brunetti G., Venturi T., Dallacasa D., Cassano R., Dolag K., Giacintucci S., Setti G., 2007, ApJ, 670, L5
Brunetti G. et al., 2008, Nature, 455, 944
Brunetti G., Cassano R., Dolag K., Setti G., 2009, A&A, 507, 661
Buote D. A., 2001, ApJ, 553, L15
Carilli C. L., Taylor G. B., 2002, ARA&A, 40, 319
Cassano R., Brunetti G., Setti G., 2006, MNRAS, 369, 1577
Cassano R., Ettori S., Giacintucci S., Brunetti G., Markevitch M., Venturi T., Gitti M., 2010, ApJ, 721, L82
Crawford C. S., Edge A. C., Fabian A. C., Allen S. W., Bohringer H., Ebeling H., McMahon R. G., Voges W., 1995, MNRAS, 274, 75
den Hartog R., Katgert P., 1996, MNRAS, 279, 349
Dennison B., 1980, ApJ, 239, L93
Dewdney P., Turner W., Millenaar R., McCool R., Lazio J., Cornwell T. J., 2013, SKA1 System Baseline Design, Document number SKA-TEL-SKO-DD-001
Ebeling H., Edge A. C., Mantz A., Barrett E., Henry J. P., Ma C. J., van Speybroeck L., 2010, MNRAS, 407, 83
Ensslin T. A., Biermann P. L., Klein U., Kohle S., 1998, A&A, 332, 395
Feretti L., 2000, preprint (arXiv:e-prints)
Feretti L., Fusco-Femiano R., Giovannini G., Govoni F., 2001, A&A, 373, 106
Feretti L., Orrù E., Brunetti G., Giovannini G., Kassim N., Setti G., 2004, A&A, 423, 111
Feretti L., Schuecker P., Böhringer H., Govoni F., Giovannini G., 2005, A&A, 444, 157

Feretti L., Bacchi M., Slee O. B., Giovannini G., Govoni F., Andernach H., Tsarevsky G., 2006, MNRAS, 368, 544
Feretti L., Giovannini G., Govoni F., Murgia M., 2012, A&AR, 20, 54
Giovannini G., Tordi M., Feretti L., 1999, New Astron., 4, 141
Girardi M., Bardelli S., Barrena R., Boschin W., Gastaldello F., Nonino M., 2011, A&A, 536, A89
Govoni F., Enßlin T. A., Feretti L., Giovannini G., 2001a, A&A, 369, 441
Govoni F., Feretti L., Giovannini G., Böhringer H., Reiprich T. H., Murgia M., 2001b, A&A, 376, 803
Hill J. M., Oegerle W. R., 1993, AJ, 106, 831
Hoeft M., Brüggen M., Yepes G., Gottlöber S., Schwope A., 2008, MNRAS, 391, 1511
Hurley-Walker N. et al., 2014, PASA, 31, 45
Hurley-Walker N. et al., 2017, MNRAS, 464, 1146
Intema H. T., 2014, preprint (arXiv:1402.4889)
Intema H. T., van der Tol S., Cotton W. D., Cohen A. S., van Bemmel I. M., Röttgering H. J. A., 2009, A&A, 501, 1185
Intema H. T., Jagannathan P., Mooley K. P., Frail D. A., 2016, A&A, preprint (arXiv:1603.04368)
Jones F. C., Ellison D. C., 1991, Space Sci. Rev., 58, 259
Juett A. M. et al., 2008, ApJ, 672, 138
Kale R., Venturi T., Giacintucci S., Dallacasa D., Cassano R., Brunetti G., Macario G., Athreya R., 2013, A&A, 557, A99
Kanov K. N., Sarazin C. L., Hicks A. K., 2006, ApJ, 653, 184
Kempner J. C., David L. P., 2004, MNRAS, 349, 385
Komissarov S. S., Gubanov A. G., 1994, A&A, 285, 27
Liang H., Hunstead R. W., Birkinshaw M., Andreani P., 2000, ApJ, 544, 686
Lonsdale C. J. et al., 2009, IEEE Proc., 97, 1497
Offringa A. R. et al., 2014, MNRAS, 444, 606
Owers M. S., Randall S. W., Nulsen P. E. J., Couch W. J., David L. P., Kempner J. C., 2011, ApJ, 728, 27
Petrosian V., 2001, ApJ, 557, 560
Pfrommer C., Enßlin T. A., 2004, A&A, 413, 17
Piffaretti R., Arnaud M., Pratt G. W., Pointecouteau E., Melin J.-B., 2011, A&A, 534, A109
Planck Collaboration VIII, 2011, A&A, 536, A8
Reiprich T. H., Böhringer H., 2002, ApJ, 567, 716
Rudnick L., Lemmerman J. A., 2009, ApJ, 697, 1341
Scaife A. M. M., Heald G. H., 2012, MNRAS, 423, L30
Slee O. B., Roy A. L., Murgia M., Andernach H., Ehle M., 2001, AJ, 122, 1172
Solovyeva L., Anokhin S., Feretti L., Sauvageot J. L., Teyssier R., Giovannini G., Govoni F., Neumann D., 2008, A&A, 484, 621
Struble M. F., Rood H. J., 1999, ApJS, 125, 35
Subramanian K., Shukurov A., Haugen N. E. L., 2006, MNRAS, 366, 1437
Sutinjo A., O'Sullivan J., Lenc E., Wayth R. B., Padhi S., Hall P., Tingay S. J., 2015, Radio Sci., 50, 52
Tingay S. J. et al., 2013, PASA, 30, 7
van Haarlem M. P. et al., 2013, A&A, 556, A2
Valtchanov I., Murphy T., Pierre M., Hunstead R., Lémonon L., 2002, A&A, 392, 795
Vazza F., Brüggen M., 2014, MNRAS, 437, 2291
Vazza F., Eckert D., Brüggen M., Huber B., 2015, MNRAS, 451, 2198
Vazza F., Brüggen M., Wittor D., Gheller C., Eckert D., Stubbe M., 2016, MNRAS, 459, 70
Venturi T., Giacintucci S., Brunetti G., Cassano R., Bardelli S., Dallacasa D., Setti G., 2007, A&A, 463, 937
Venturi T., Giacintucci S., Dallacasa D., Cassano R., Brunetti G., Bardelli S., Setti G., 2008, A&A, 484, 327
Venturi T., Giacintucci S., Dallacasa D., Cassano R., Brunetti G., Macario G., Athreya R., 2013, A&A, 551, A24
Wayth R. B. et al., 2015, PASA, 32, e025

This paper has been typeset from a TEX/LATEX file prepared by the author.